analytical chemistry

pubs.acs.org/ac Article

Advanced SERS Platform for Uniform and Reliable Molecular Detection

Tiying Zhu, Zhiyang Pei, Xiaofei Zhao, Jing Yu, Baoyuan Man, Pingheng Tan, Zhen Li,* and Chao Zhang*

Cite This: *Anal. Chem.* 2024, 96, 20612−20621 Read Online

ACCESS | Metrics & More | Article Recommendations | Supporting Information

ABSTRACT: Signal uniformity is crucial for reliable and quantifiable surface-enhanced Raman scattering (SERS) measurements. However, challenges arise due to the continuous impact of localized hottest spots and the coffee ring effect on signal uniformity. In response to this, we developed a platform featuring a hierarchical structure with Ag nanopores and microbowls (HANM) and incorporated superhydrophobic/superhydrophilic (SHB/SHL) treatments. This design enhances the hottest spot area, ensuring a strong and consistent electromagnetic field while mitigating the coffee ring effect, which leads to an even analyte distribution. This was demonstrated by analyzing rhodamine 6G (R6G, 4 μL, 10^{-9} M to 10^{-12} M) molecules at different concentrations. The 2D mapping of the SERS signal intensities from the entire dried droplet exhibited excellent uniformity. The relative standard deviation of the intensities from 200 randomly selected points was calculated to be just 3.81%, laying the foundation for the quantitative detection capability. Additionally, through bisphenol A (BPA) detection in water samples collected from five different locations, the HANM-SHB/SHL structure consistently detected BPA with a uniform signal intensity across all water samples. In conclusion, we proposed a dual-function SERS platform featuring an improved hottest spot region and the ability to avoid the coffee ring effect, offering precise and reliable molecular analysis.

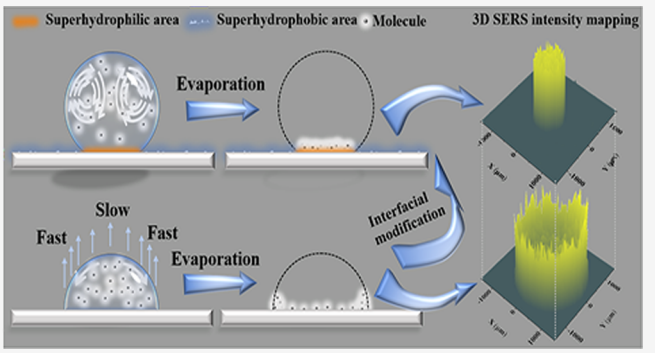

INTRODUCTION

Surface-enhanced Raman scattering (SERS) as a molecular detection technique with immense potential showcases versatile attributes like label-free detection, swift response, exceptional selectivity, and heightened sensitivity,[1−6] which has been widely utilized in diverse fields such as food safety, environmental monitoring, biomedicine, and analytical chemistry through nanoscale interactions with silver (Ag) or gold (Au) nanostructures.[7−11] However, the nanogaps formed between Ag or Au nanostructures, referred to as "hottest spot", exhibit localized characteristics.[12] This inherently gives rise to the nonuniformity of detection signals, posing challenges to quantitative capabilities. While diversified methods such as the introduction of molecular adapters or surface modifications can be employed to influence hotspot generation, in practical applications, hottest spots typically remain a pivotal factor for attaining heightened sensitivity in SERS technology.[13,14] Consequently, the design of novel nanostructures becomes imperative to realize a more uniform electric field distribution, aiming to strike a delicate balance between fostering hottest spot generation and controlling their nonuniform characteristics.

On the other hand, the reliability of SERS technology is intricately tied to the uniform distribution of analytes. However, the pervasive influence of the coffee ring effect causes a majority of analytes to preferentially accumulate at the outer edges of liquid droplets.[15] Over time, the accumulation of ring-shaped bands on the SERS substrate creates instability in the signal strength, challenging the reliability of molecular signals and hindering the precision of quantitative molecular diagnostics.[16] In response to this challenge, researchers have embarked on a multifaceted journey employing a myriad of strategies. These include the fine-tuning of substrate surface structures, the integration of micronanostructures, the meticulous adjustment of droplet concentrations, and the application of cutting-edge microfluidic techniques.[17−20] The collective aim is to augment the uniform distribution of analytes, ushering in a marked improvement in the quality and

Received: September 30, 2024
Revised: November 26, 2024
Accepted: December 6, 2024
Published: December 18, 2024

https://doi.org/10.1021/acs.analchem.4c05301
Anal. Chem. 2024, 96, 20612−20621

precision of signals within SERS technology. However, the optimization processes in SERS technology often overlook the intricate interactions among analyte molecules, substrates, and air during the drying process, which are crucial for enhancing the signal intensity. The intricacies of these interactions, involving factors such as solvent evaporation, molecular diffusion, and surface tension, may lead to an uneven distribution of analytes in the final solidified state, thereby impacting the desired uniformity of the signals. Therefore, in the optimization design, meticulous control of these intricate interactions during the drying process becomes crucial to ensure consistency and reliability of the final SERS signals.

In this research, we propose a novel SERS platform aimed at enhancing the uniformity of SERS signals by integrating a hierarchical Ag nanoporous/microbowl (HANM) structure and a superhydrophobic/superhydrophilic (SHB/SHL) surface treatment (Figure 1). This innovative design addresses both structural and molecular distribution aspects to promote the uniformity of SERS signals. The intricately crafted HANM structure acts as a sophisticated optical amplifier, capturing and leveraging incident light multiple times.[21,22] The resultant cascade of optical field modes, generated through the coupling of nanopores and microbowls, transforms the entire nanopore into the uniformity hottest spot region. This designed enhancement can significantly elevate both the intensity and the uniformity of SERS signals. On the flip side, the SHB/SHL mode serves as a pivotal component, orchestrating a templated point-by-point construction of SHL sites on the SHB platform. The formation of these hydrophilic regions offers a trio of advantages. First, owing to its SHB nature, analyte droplets exhibit an autonomous tendency to contract toward specific hydrophilic areas, eliminating the laborious need for microscopic point-by-point searches to locate analyte presence. Second, the strategically positioned hydrophilic sites serve as effective constraints, limiting the dispersed area of added analyte molecules and facilitating analyte enrichment. Lastly, and perhaps most crucially, the SHB/SHL mode exerts its influence by enhancing the Marangoni effect. This augmentation effectively suppresses the coffee ring effect, mitigating the outward flow of analytes induced by the capillary action. This multifaceted approach not only showcases the subtlety of the microstructure design but also addresses key challenges associated with SERS technology, offering a promising avenue for advancing the reliability, sensitivity, and application potential of SERS platforms.

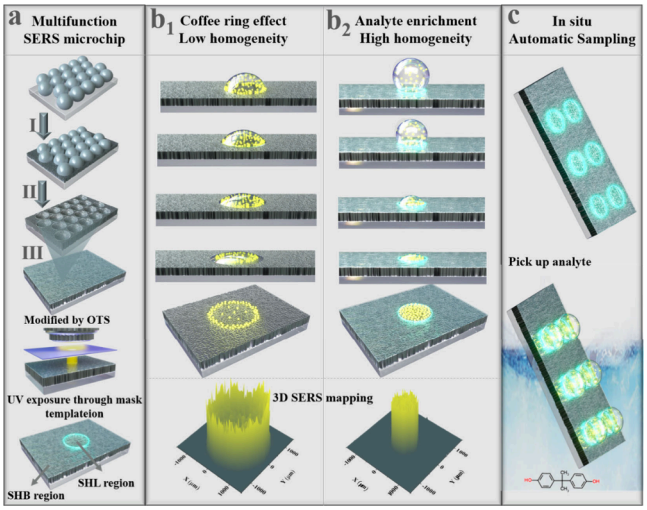

Figure 1. (a) Schematic diagram of the synthesis process of the HANM-SHB/SHL structures (I, electrochemical deposition; II, removal of PS microspheres; III, local zoom). (b_1, b_2) On the HANM and HANM-SHB/SHL structures, the droplet drying process. The 3D SERS mapping height and distribution size measured by droplet drying on the two structures can clearly compare the difference between the two modes. (c) Conceptual diagram of in situ molecular pickup and targeted enrichment.

EXPERIMENTAL SECTION

Apparatus and Reagents. Indium tin oxide (ITO) conductive glass with a resistance of 6 ohms was purchased from South Xiangcheng Technology. 5 wt % polystyrene (PS) microspheres were purchased from Ganzhou Mike Xin Technology Co., Ltd. Silver nitrate ($AgNO_3$), citric acid ($C_6H_8O_7$), toluene (C_7H_8, AR, ≥99.5%), and ethanol (C_2H_6O, AR, ≥99.5%) were obtained from China Pharmaceutical Chemical Reagent Co., Ltd. Sodium dodecyl sulfate (SDS), octadecyltrichlorosilane (OTS), and BPA were purchased from Shanghai Aladdin Biochemical Technology Co., Ltd. All materials have not undergone further purification.

The HANM-SHB/SHL structure was prepared by using an electrochemical workstation (CHI 760E) with a fixed current density of 180 $\mu A/cm^2$ for electrochemical deposition. The morphology of the HANM-SHB/SHL structure was revealed through scanning electron microscopy (SEM, ZEISS Sigma500) and atomic force microscopy (AFM, SmartSPM). The absorption spectra (A) were measured using a UV−visible spectrophotometer (Shimadzu Solid Spec-3700i), and SERS spectra for different probe molecules were collected using a Raman spectrometer (Horiba HR Evolution 800). Laser wavelength, laser power, integration time, and magnification were set at 532 nm, 0.4 mW, 8 s, and 50×, respectively, unless otherwise specified.

Preparation of Monolayer Colloidal Crystal (MCC) Template. The MCC template, comprised of 2 μm PS microspheres, was fabricated through a self-assembly process. Initially, glass slides underwent oxygen plasma treatment at 50 W power for 3 min to induce superhydrophilicity on their surfaces. Subsequently, 30 μL of a mixture of PS microspheres and ethanol at a volume ratio of 1:1 was taken and dropped onto the plasma-treated slides and allowed to diffuse freely. Following natural drying, the inclined glass slide was immersed in a solution containing 500 μL of 2 wt % SDS in 500 mL of deionized water. Under the influence of SDS, the PS microspheres progressively dissociated from the glass slide surface, organizing into a meticulously arranged monolayer array floating at the air/water interface. Next, an ITO conductive glass substrate was employed to retrieve and assemble the PS microspheres array. The system was then subjected to a 10 min heating process at 60 °C on a heating stage, promoting the tight adhesion of PS microspheres to the ITO conductive glass surface and culminating in the formation of the MCC template. Schematic diagram of PS microsphere template preparation is shown in Figure S1.

Preparation of the HANM Structure. The HANM structure was prepared using an electrochemical deposition method with an MCC array as the template. Under a constant current of 180 $\mu A/cm^2$, electrodeposition was conducted in a solution containing 1.4 g of citric acid and 0.16 g of 80 mL of water using a water bath heating method. During the

https://doi.org/10.1021/acs.analchem.4c05301
Anal. Chem. 2024, 96, 20612−20621

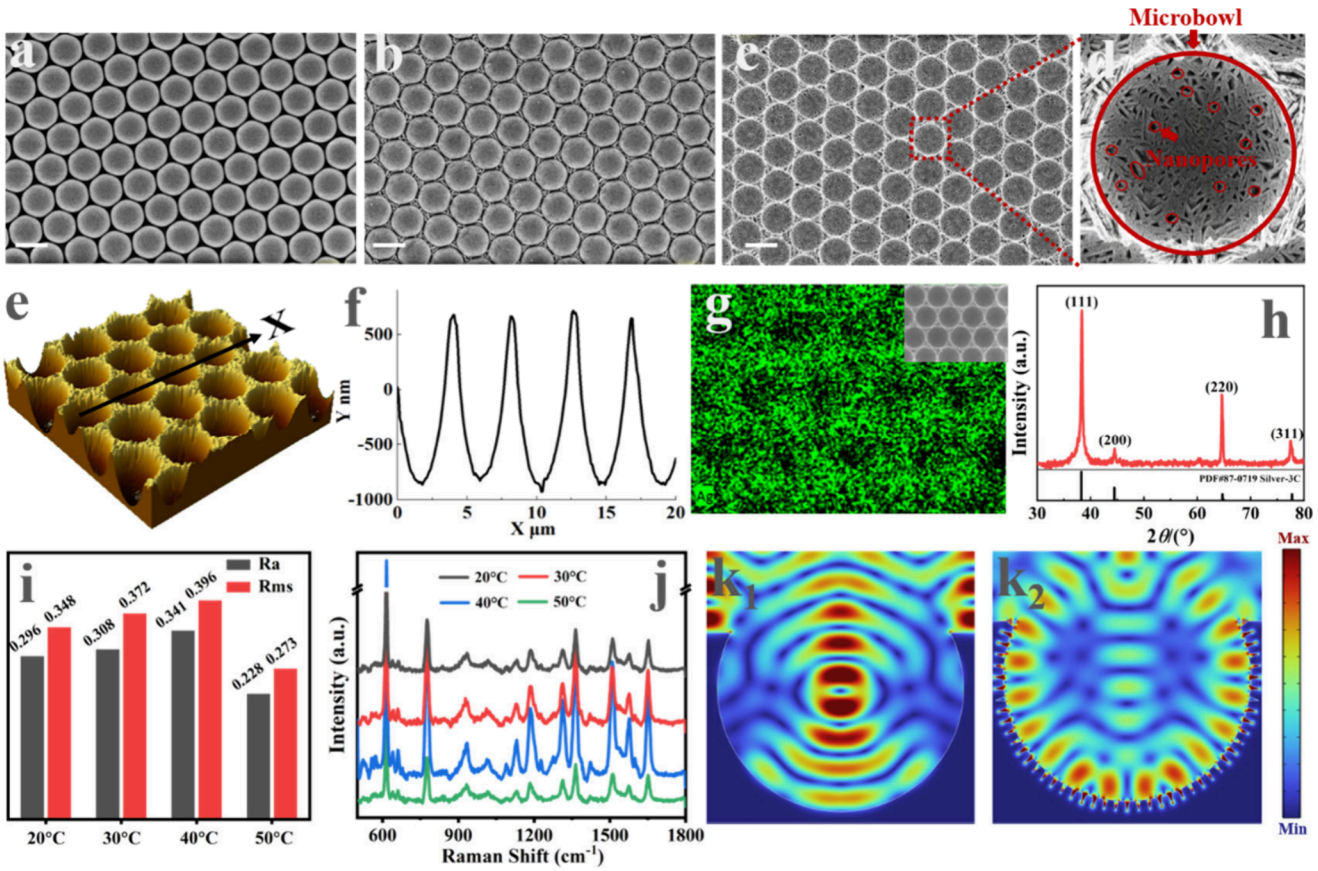

Figure 2. (a–d) SEM images of PS microsphere arrays, PS microsphere arrays after electrochemical deposition, HANM structures, and localized magnification of HANM structures. The scale is 2 μm. (e) AFM image of the HANM structure. (f) Line profile corresponding to the position of the black marked line in (e). (g) EDS images of HANM structures (the scale is 2 μm). (h) XRD of HANM structures. (i) Ra and Rms of different samples prepared under different conditions. (j) SERS spectra collected from AM structures prepared at different temperatures. (k) COMSOL simulated electric field distribution of AM and HANM structures.

electrodeposition process, a graphite rod served as the anode, while the MCC template acted as the cathode. The reaction temperature was maintained at 40 °C, and the electrodeposition process was sustained for a total duration of 70 min. After completion of the reaction, the array was washed sequentially with ethanol and ultrapure water followed by drying. Subsequently, it was immersed in a solution of toluene for 6 h. The PS microspheres were completely removed during this process, resulting in the fabrication of an array of HANM. When illuminated by a point light source, the structured patterns (as depicted in Figure S2) exhibit systematic color variations due to light diffraction. This effect emphasizes the pronounced periodicity of the Ag nanopores–microbowls structure.

Preparation of the HANM-SHB/SHL Structure. The preparation of the SHB/SHL pattern followed the method reported by Wang et al.[23] Initially, the HANM structure was immersed in a 1% OTS solution, where the solvent used was anhydrous toluene, and the treatment lasted for 30 min. Subsequently, excess OTS was removed through alternating rinses with toluene and ethanol. Next, the OTS-modified HANM structure was covered with a photomask and exposed to ultraviolet (UV) light from a high-pressure mercury lamp for 3 h. Due to the photodegradation of the OTS, the region subjected to UV irradiation exhibited SHL properties, while the untreated region retained its SHB characteristics. Through this treatment, the formation of an alternating SHB/SHL pattern was achieved. The initial contact angles of 4 μL droplets on the substrate were 85.9° (untreated), 154.6° (OTS-modified), and 6.7° (OTS-modified under UV exposure) (see Figures S3). This indicates that the successful formation of SHB/SHL alternating surfaces on the silver nanopore microbowl array can be achieved through OTS modification followed by selective UV irradiation.

COMSOL Simulation. COMSOL is a multiphysics simulation software based on the finite element method (FEM), which solves numerical problems by discretizing continuous systems into finite elements. This simulation utilizes COMSOL's wave optics module to accurately compute the electromagnetic field distribution of the HANM structure. The focus is on a single HANM structure with an incident plane wave propagating along the *Z*-axis. To simulate an infinite periodic array structure and minimize errors caused by edge effects, periodic boundary conditions (PBCs) were applied along the *X* and *Y* axes. Perfectly matched layers (PMLs) were used in all directions to absorb outgoing waves and prevent boundary reflections, ensuring that electromagnetic wave propagation within the finite space replicates the physical behavior at infinite distances. This simulation employed a wavelength domain study to solve Maxwell's equations under harmonic excitation. The excitation wavelength was set to 532 nm to match the experimental conditions. The mesh was configured with a maximum element size of 66 nm and a minimum element size of 0.1

https://doi.org/10.1021/acs.analchem.4c05301
Anal. Chem. 2024, 96, 20612–20621

nm with a growth rate of 1.1. Local mesh refinement was applied in regions with strong electromagnetic field gradients, particularly near the surface of the nanostructure, to ensure the solution accuracy in critical areas. In terms of material properties, the optical constants of silver were taken from Johnson and Christy's experimental data to accurately model plasmonic effects. The refractive index of the surrounding medium was also set according to experimental conditions to ensure consistency between the simulation results and experimental observations.

RESULTS AND DISCUSSION

Characteristics of the Substrate. The HANM structure plays a vital role in enhancing light-capturing capabilities, which has profound significance in the field of SERS. Among the various methods for preparation, electrochemical deposition stands out due to its controllability and cost-effectiveness, making it a preferred choice in SERS research. The orderly array of PS microspheres shown in Figure 2a served as templates for subsequent Ag deposition. As the electrochemical reaction proceeded, Ag nanoparticles were deposited in the gaps between adjacent PS microspheres (Figure 2b). Upon reaching a certain deposition time, the PS microspheres were removed, resulting in an array of HANM structures, as shown in Figure 2c. The magnified view in Figure 2d clearly displays the microbowls and nanopores within the AM structure, confirming the successful fabrication of this microbowls structure. To better understand the morphology and characteristics of these structures, various characterizations were conducted. The 3D AFM image (Figure 2e) shows the uniform arrangement of the microbowl structures, while the periodic profile variations along the *X*-axis in Figure 2f, corresponding to the position of the black marked line in Figure 2e, further highlight the uniformity and consistency of the microbowl structures in terms of height, confirming that the height of each microbowl is approximately 1.6 μm. Additionally, the slight undulations at the bottom of the profile once again verify the presence of nanoscale pores. EDS images (Figure 2g) and XRD spectra (Figure 2h) were used to confirm the distribution of Ag elements within these microbowl structures, verifying the successful fabrication of the HANM structure.

In further studies, the effects of varying electrochemical deposition times on the morphology and properties of HANM structures were investigated. SEM images taken at deposition times of 30, 50, 70, and 90 min illustrated the evolution of these structures (Figure S4). In the cross-sectional SEM images of AM structures with varying deposition times, a significant change in HANM height can be observed. Through measurement and analysis of the cross sections of HANM structures at different deposition times, the relationship between HANM height (H) and time (T) can be summarized as $H = -0.16T^2 + 41.51T - 565.4378$ (Figure S4e). Optimizing deposition time not only enhanced SERS signals but also provided crucial design insights for the development of other nanostructure-based optical devices. SERS analysis using R6G as a model compound demonstrated that the HANM structure exhibited the strongest SERS signal when deposited for 70 min with a depth of 1.6 μm (Figure S4f). This optimization was attributed to achieving an optimal balance between nanopore formation and structural height, effectively enhancing the necessary plasmonic effects and thus boosting the SERS signal enhancement.

The electrolyte temperature is another critical factor influencing the morphology of electrochemically deposited structures. Figure S5 shows SEM images of Ag microbowl (AM) structures deposited at temperatures ranging from 20 to 50 °C. At 20 °C, the inner surface of the AM structure is relatively smooth and flat; at 30 °C, the surface becomes increasingly rough, with internal gaps appearing; at 40 °C, these gaps become more pronounced, forming extensive nanopores surrounded by nanosheets; and at 50 °C, the nanosheets thicken into plates, reducing the number of nanopores. The effects of these temperature changes can be explained by the Arrhenius equation, which describes the relationship between chemical reaction rate and temperature:

$$k = A^{-E_a/(RT)}$$

where k is the reaction rate constant, A is the frequency factor, E_a is the activation energy, R is the gas constant, and T is the absolute temperature. Higher temperatures accelerate the reduction rate of Ag ions, affecting crystal formation and altering the structure of the AM.[24,25]

Absorption spectra of substrates prepared at different temperatures show a gradual increase in light absorption at 20 °C, 30 °C, and 40 °C, attributed to the formation of nanopores that enhance the optical path length and thus increase light absorption (Figure S5). However, at 50 °C, although nanopores are still present, the thicker nanosheets reduce the number of nanopores, thereby affecting the light absorption efficiency. Surface roughness (Ra) and root-mean-square roughness (Rms) of SERS substrates prepared at different temperatures are shown in Figure 2i. It is noteworthy that the trends in Ra and Rms correlate with the intensity of the absorption spectra, highlighting the crucial role of surface morphology in light capture. To further elucidate the mechanism of nanopore-enhanced SERS effects, COMSOL simulations were employed to model the electromagnetic field distribution in smooth microbowls and HANM. Based on SEM image statistics, nanopores were characterized with dimensions of 77.5 nm and gaps of 32.5 nm (Figure S6). Simulation results demonstrate that nanopores effectively concentrate the electromagnetic field (Figure 2k$_2$), which not only avoids the generation of the hottest spot but also increases the intensity of the concentrated distribution of the electric field in the nanopores. Although smoother bowl centers exhibit stronger electric field distributions (Figure 2k$_1$), their contribution to molecular enhancement of the bowl walls is minimal. SERS spectra of the AM structure at different temperatures (Figure 2j) further confirm the positive impact of nanopores, with samples at 40 °C exhibiting optimal performance. The hierarchical Ag structure formed by nanopores and Ag microbowls (HANM) at 40 °C establishes a solid foundation for future research in hierarchical micronano optical cavities.

Droplet Drying Processes in HANM and HANM-SHB/SHL, along with the Working Principles of the HANM-SHB/SHL Structure. In the application of SERS technology, it is crucial not only to avoid the generation of the hottest spots but also to ensure uniform distribution of analytes. To mitigate the negative effects of the coffee ring effect, which leads to uneven molecular distribution, we adopted an innovative strategy by preparing an SHB/SHL interactive surface. This approach ensures a uniform distribution of analytes on the substrate. The HANM structure was immersed in a toluene solution of OTS for 30 min to achieve SHB performance. After

https://doi.org/10.1021/acs.analchem.4c05301
Anal. Chem. 2024, 96, 20612−20621

OTS modification, the contact angle of the HANM structure reached 154.6°, as shown in Figure S3b. On the OTS-functionalized HANM structure, UV exposure through a photomask achieved controllable modulation of hydrophilic sites. Following a 3 h UV exposure, the OTS alkyl chains beneath the UV-irradiated region undergo decomposition, yielding polar hydrophilic oxygen moieties, including aldehydes and carboxylic acid salts.[26−28] This process results in the creation of a surface with SHB/SHL properties.

In order to investigate the impact of SHB/SHL interactive surfaces on the droplet deposition process, R6G was employed as the analyte (concentration of 10^{-7} M, 4 μL) to reveal the differences in distribution during the evaporation process and postevaporation stages on the HANM-SHB/SHL structure compared to the HANM structure (front view, Figure 3b,c; top view, Figure S7). Experimental results showed that droplets of the R6G solution on the HANM structure exhibited an initial hemispherical shape. As evaporation progressed, R6G molecules primarily deposited along the periphery of the droplets, forming a distinct ring-shaped distribution. Within this annular region, the molecular concentration surpassed that of the central part of the droplet, exhibiting a pronounced coffee ring effect, with the diameter of the coffee ring reaching 2 mm. In contrast, on the HANM-SHB/SHL structure, droplets assumed a nearly spherical shape within the anchored hydrophilic regions. It is noteworthy that compared to the HANM structure, the evaporation rate of R6G solution droplets was significantly decelerated in this scenario. Following the conclusion of the evaporation process, it was surprising to observe a remarkably uniform distribution of the analyte within the hydrophilic zone. The resulting deposition spot diameter was merely 1 mm, perfectly aligning with the dimensions of the hydrophilic region.

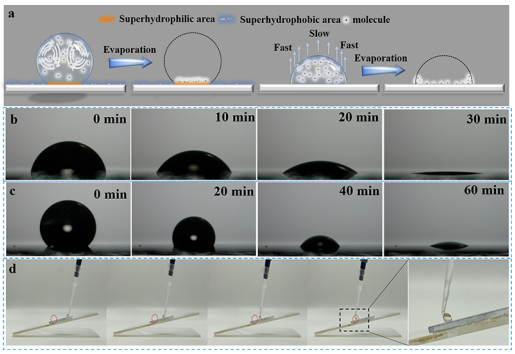

Figure 3. (a) Schematic illustration of droplet evaporation on the HANM-SHB/SHL and HANM structure. Optical image of droplet evaporation on (c) HANM-SHB/SHL structure and (b) HANM structures. (d) Optical images of droplet states at SHB and SHB/SHL site.

It is evident that the deposition behavior of the droplet is closely related to the wetting properties of the substrate. On the HANM structure, the evaporation of R6G solution droplets adheres to a constant contact area model, with the contact line fixed at the substrate. As the droplet evaporates, its height decreases, leading to a decrease in the contact angle. The relatively larger surface area-to-volume ratio at the droplet's edge results in a higher evaporation rate at the periphery than at the center.[29] This prompts a continuous supply of solution from the center to the periphery, causing the constant movement and deposition of R6G molecules at the periphery and ultimately forming a pronounced coffee ring (Figure 3a, right). For the HANM-SHB/SHL structure, outward flow still occurs, but the evaporation-induced Marangoni effect leads to a predominant recirculating flow.[30] The strength of the Marangoni effect correlates with droplet height-higher droplets exhibit faster recirculating flow.[31] The R6G droplet, anchored within the SHL region, maintains a stable spherical shape with a heightened droplet due to a smaller contact area, intensifying the Marangoni-induced recirculating flow. Simultaneously, the spherical droplet shape reduces edge evaporation and weakens the outward flow. When the R6G droplet contacts the SHL Ag nanopore-microbowl structure, capillary action facilitates solution penetration into the microstructure, akin to liquid rising in a straw. This enhances the comprehensive entry of the solution into the microstructure beyond surface confinement. The porous structure imposes significant hydrodynamic resistance to outward flow at the droplet's edge, creating a metaphorical "resistance wall" that inhibits outward flow. Consequently, recirculating flow takes precedence during droplet evaporation, preventing the coffee ring effect and guiding dissolved substances to the droplet center, resulting in a distinct and uniformly deposited spot (Figure 3a, left). This unique droplet dynamic effect robustly supports achieving an even distribution of analytes on the HANM-SHB/SHL structure.

The SHB/SHL interactive surface plays a positive role in promoting high-throughput SERS detection. Utilizing photomasks allows the creation of an array of hydrophilic sites at specific locations, greatly facilitating the handling of numerous samples and conducting multiple analyses. While some studies utilize SHB interfaces to achieve the enrichment of analytes, which to some extent mitigates the impact of the coffee ring effect, several challenges persist in practical detection. For instance, the manual positioning of detection points for trace molecules after evaporation introduces subjectivity and an additional workload. Additionally, on SHB surfaces, droplets tend to exhibit noticeable oscillations upon slight external forces, making precise control during the evaporation process challenging. The creation of hydrophilic regions on SHB surfaces allows for the anchoring of analytes in an array format at fixed locations. As illustrated in Figure 3d, we placed the HANM-SHB/SHL structure on a platform inclined at a 15° angle and then introduced a droplet into the SHB region. The droplet rapidly slid, but upon reaching the fixed SHL region (as indicated by the red circle), even when the pipet tip formed a certain traction angle with the droplet, the contact position between the droplet and the substrate remained unchanged. The figure displays an array of analytes on the SHB/SHL interactive surface. By designing the wettability of the target regions, this interactive surface streamlines the entire detection process, promising a more significant role in high-throughput analysis (Supporting Information Movies 1 and 2).

SERS Properties of the HANM-SHB/SHL Structure. To understand the influence of SHB/SHL interactive surfaces on HANM structure SERS sensors, SERS intensity mappings of R6G molecules at 613 cm^{-1} were collected with a step size of 40 μm across a 3 × 3 mm^2 area. The 2D mapping (Figure 4a) obtained on the HANM-SHB/SHL structure for all concentrations (10^{-8} M to 10^{-12} M) shows minimal color variation, indicating the uniformity of the SERS signals. Despite fluctuations in corresponding SERS signal intensities (Figure 4b), likely due to uneven nanopore distribution, these fluctuations are relatively minor compared with overall

https://doi.org/10.1021/acs.analchem.4c05301
Anal. Chem. 2024, 96, 20612−20621

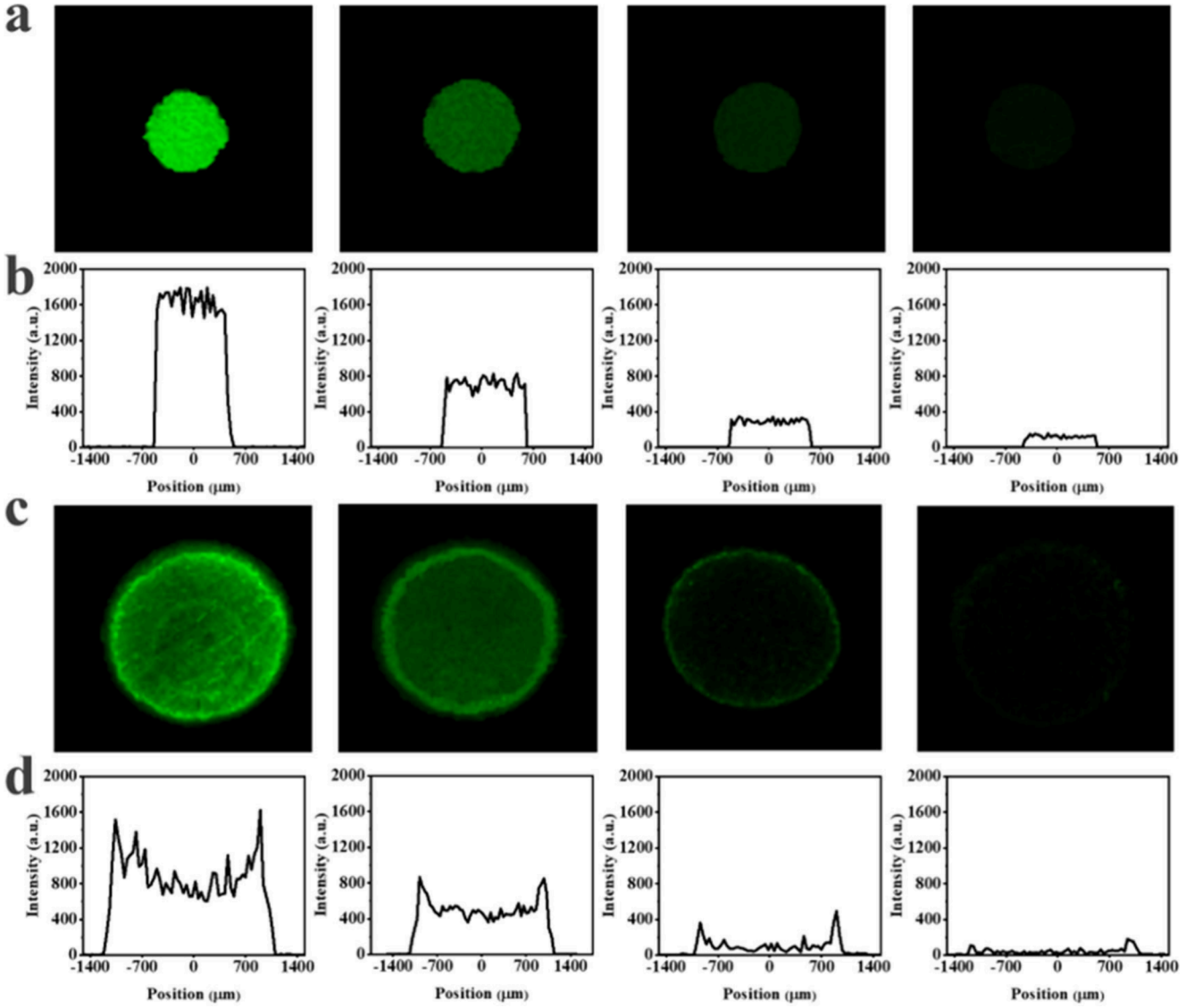

Figure 4. SERS mapping of 4 μL R6G droplets at 613 cm^{-1} obtained at different concentrations (10^{-9} M to 10^{-12} M) on (a) the HANM-SHB/SHL structure and (c) the HANM structure. (b, d) SERS intensities of the corresponding (a) and (c).

intensity. In high concentration molecular detection, despite some local irregularities in molecular distribution, sufficient SERS signal intensity is detected even in noncoffee ring areas, owing to the higher molecular presence. However, at low concentrations, the nonuniform distribution on the liquid drop surface may lead to a relative scarcity of molecules in local areas, resulting in signal attenuation or loss. Therefore, in SERS, the uniformity of surface enhancement effects is crucial for detecting low-concentration molecules. Surprisingly, under the synergistic action of the HANM structure and SHB/SHL interactive surfaces, mapping shows competitive uniformity even at concentrations as low as 10^{-12} M. Conversely, mappings obtained on the HANM structure (Figure 4c) exhibit significant uniformity defects, particularly at R6G spots with concentrations of 10^{-11} and 10^{-12} M. In these areas, intensities in central parts are almost indistinguishable from noise, highlighting challenges in uniformity at low concentrations. Additionally, the corresponding SERS signal intensities (Figure 4d) display pronounced fluctuations resembling a well shape, potentially leading to varying molecular intensities in repeated measurements at the same concentration.

The SERS intensity mapping of 10^{-10} M R6G molecules at 613 cm^{-1} obtained from three different batches is shown in Figure S8. The mapping obtained with the HANM-SHB/SHL structure exhibits a consistent size and uniform color distribution (see Figure S8a), with signal intensities also being relatively similar (see Figure S8b). This result strongly demonstrates the efficiency and excellent reproducibility of the HANM-SHB/SHL structure in molecular regulation. In contrast, the mapping obtained using HANM structures from different batches shows noticeable nonuniformity. This is particularly evident in the differences in the shape of the image areas and the inconsistency in the coffee ring shapes (see Figure S8c). The variation is clearly reflected in the intensity curves (see Figure S8d). This phenomenon is primarily due to the asymmetric shape of the droplets during deposition. During the evaporation process, the asymmetry of the droplets affects the solvent evaporation rate and particle distribution, resulting in uneven particle deposition in different regions and consequently causing variations in the shape and color of the coffee rings. Therefore, the coffee ring effect can significantly impact the reproducibility and accuracy of the detection

https://doi.org/10.1021/acs.analchem.4c05301
Anal. Chem. 2024, 96, 20612−20621

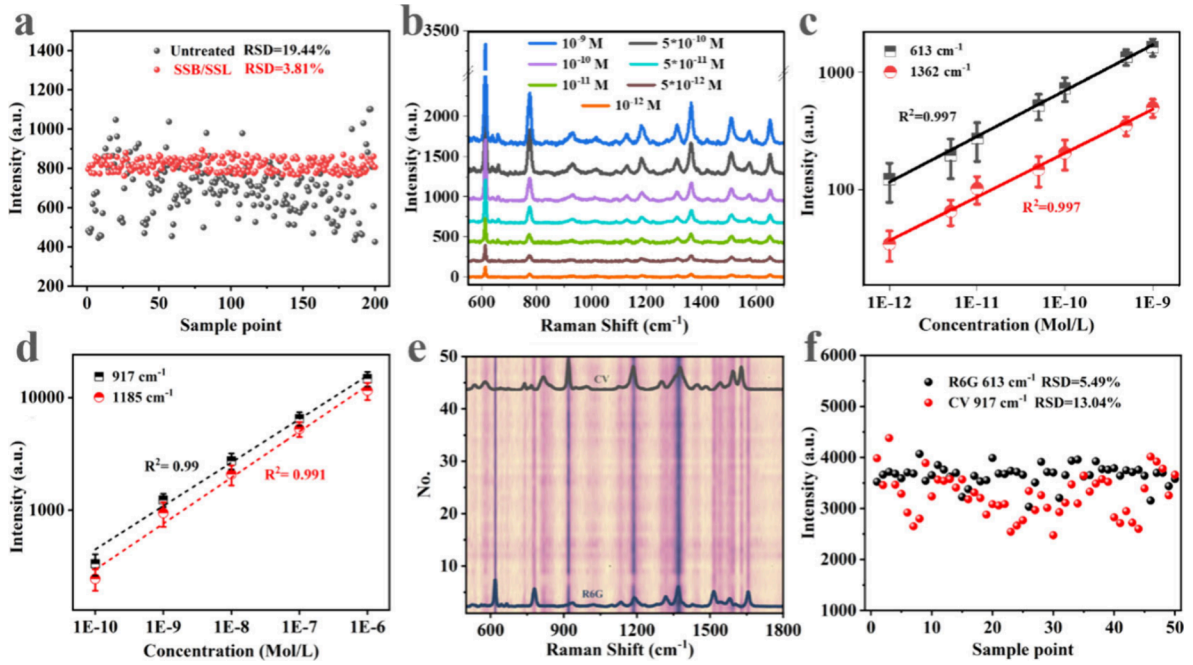

Figure 5. (a) 200 intensity scatter plots at 613 cm^{-1} for R6G molecules obtained on HANM and HANM-SHB/SHL structure. (b) SERS spectra of R6G at concentrations of 10^{-9} M to 10^{-12} M collected from HANM-SHB/SHL structure. (c) The linear relationship between SERS intensity and concentration at 613 and 1362 cm^{-1} of the R6G molecule. (d) The linear relationship between SERS intensity and concentration at 917 and 1185 cm^{-1} of the R6G molecule. (e) SERS spectral mapping of mixed R6G and CV molecules. (f) Intensity scatters for R6G molecules at 613 cm^{-1} and CV molecules at 917 cm^{-1}.

results. The HANM-SHB/SHL structure effectively overcomes this problem for analyte droplet control.

To further investigate the HANM-SHB/SHL structure on the performance of SERS sensors, a more detailed exploration of the SERS performance was conducted. A total of 200 SERS spectra covering the entire dried spot of R6G molecules were collected (Figure S9). The corresponding intensity scatter plot at 613 cm^{-1} (Figure 5a) shows that the relative standard deviation (RSD) of the SERS signal on the untreated substrate is 19.44%, while on the SHB/SHL modified substrate, the RSD significantly decreases to 3.81%. This clearly indicates that SHB/SHL modification significantly enhances the uniformity of the SERS signal. Figure 5b shows the SERS spectra collected on the HANM-SHB/SHL structure for R6G concentrations ranging from 10^{-9} to 10^{-12} M. The distinct signal peaks at different concentrations validate the high sensitivity and reliability of the HANM-SHB/SHL structure. Additionally, the SERS signal intensity at 613 and 1362 cm^{-1} shows a strong linear correlation with concentration, with R^2 values of 0.997 (Figure 5c), demonstrating the method's excellent detection performance across different concentration ranges.

Similarly, 100 SERS spectra of CV molecules on the HANM-SHB/SHL structure were collected. The SERS spectra and the corresponding intensity scatter plots at 917 and 1185 cm^{-1} (Figure S10a,b) show minimal fluctuations, with standard deviations of 2.72% and 4.43%, respectively. The consistently low standard deviations for CV molecules, similar to those of R6G molecules, suggest that the SHB/SHL-modified substrate maintains a uniform efficacy across different analytes. For the SERS spectra of CV molecules in the concentration range of 10^{-6} M to 10^{-10} M (Figure S10c), the correlation coefficients between intensity and concentration at 917 and 1185 cm^{-1} are 0.990 and 0.991 (Figure 5d), respectively, indicating a robust linear relationship between SERS peak intensity and molecule concentration. The strong linear relationships between the concentrations and intensities of R6G and CV molecules underscore the reliability of uniform SERS signals in enhancing the quantitative detection capability of SERS technology.

A mixture of R6G and CV molecules was dropped onto the HANM-SHB/SHL structure to further explore its potential for multicomponent solution detection. By collecting 50 SERS spectra of the multicomponent molecules, a mapping was created, with characteristic peaks perfectly matching those in the individual R6G and CV spectra (Figure 5e). This confirms that the HANM-SHB/SHL structure are capable of multicomponent analysis and suitable for complex sample analysis. The corresponding RSD values of the characteristic peaks at 613 cm^{-1} for R6G and 917 cm^{-1} for CV in the mixed molecule spectra are 5.49% and 13.07% (Figure 5f), respectively. The increased RSD values compared to single-molecule detection could be due to different molecules competing for the same SERS-active sites in the mixture, resulting in reduced adsorption in certain regions and causing fluctuations in signal intensity and uniformity. Additionally, interactions between different molecules, such as hydrogen bonding and van der Waals forces, may alter their distribution on the substrate. These interactions can lead to some molecules aggregating, while others disperse, affecting signal uniformity. Despite this, the RSD values for multicomponent detection are well below the scientific standard of 20% reported by Natan.[32] Such uniformity is crucial for ensuring the reliability and repeatability of detection results, especially in applications requiring precise quantitative analysis, such as environmental monitoring and biomedical analysis.

The HANM-SHB/SHL Structure Applications. The development of the HANM-SHB/SHL structure represents a direct and effective method for fabricating high-precision and

https://doi.org/10.1021/acs.analchem.4c05301
Anal. Chem. 2024, 96, 20612−20621

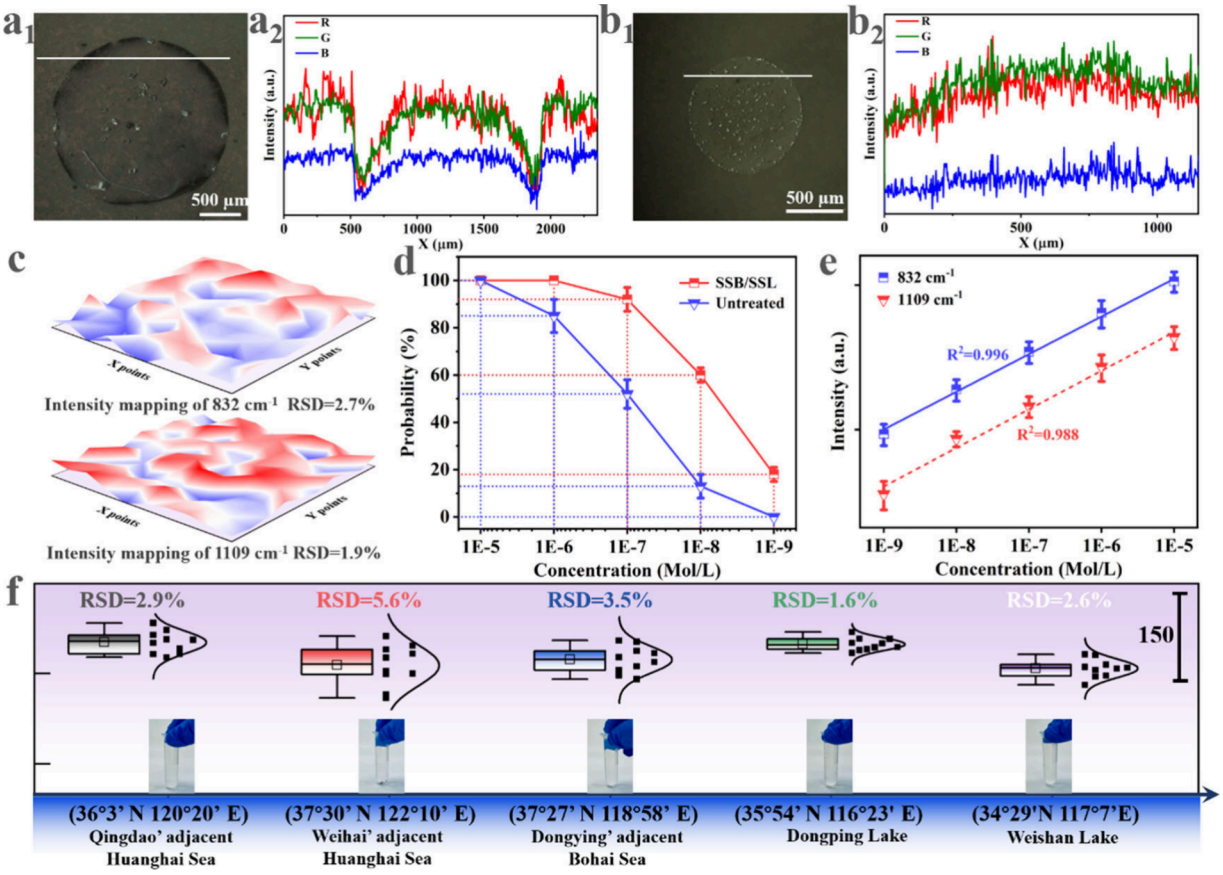

Figure 6. (a_1, a_2) Optical images and corresponding color scale changes of BPA molecular droplets drying on HANM structure. (b_1, b_2) Optical images and corresponding color scale changes of BPA molecular droplets drying on HANM-SHB/SHL structure. (c) SERS intensity mapping of peaks 832 and 1109 cm^{-1}. (d) The probability of obtaining observable SERS signals at different concentrations on HANM and HANM-SHB/SHL structure. (e) The linear relationship between SERS intensity and concentration at 832 and 1109 cm^{-1} of BPA. (f) SERS intensity distribution of BPA molecules at 832 cm^{-1} in water samples from five locations using the HANM-SHB/SHL structure: Qingdao' adjacent Huanghai Sea, Weihai' adjacent Huanghai Sea, Dongying' adjacent Bohai Sea, Dongping Lake and Weishan Lake, based on 10 randomly collected SERS spectra from each site.

highly sensitive SERS chips. This approach has been successfully demonstrated through promising results in the detection of dye molecules (R6G, CV). Persistent organic pollutants, which are typically weakly adsorbed molecules commonly found in surface and groundwater,[33,34] pose challenges for SERS detection due to their low scattering cross sections. To validate the practical application capability of the HANM-SHB/SHL structure, BPA was chosen as the target molecule for further investigation.

On the HANM structure, optical microscopy images revealed that the BPA droplet formed a distinct coffee-ring spot (Figure 6a1). The grayscale changes corresponding to the line in Figure 6a1 intuitively reflected the diameter and molecular distribution of the dried spot (Figure 6a2). The significant fluctuations in RGB intensity at the edges of the dried spot confirmed the large accumulation of molecules at the edges, leading to an uneven molecular distribution and making it difficult to obtain accurate and sensitive SERS signals. In contrast, on the HANM-SHB/SHL structure, the BPA droplet formed relatively uniform spots (Figure 6b1), as verified by the low intensity undulation of the grayscale curve over the entire molecular coverage area (Figure 6b2). Due to the improved uniformity of molecular distribution and the smaller spot diameter compared to the HANM structure, the HANM-SHB/SHL structure was able to achieve sensitive and accurate SERS signals.

SERS spectra (Figure S11a) of 100 randomly selected points on uniformly spotted BPA molecules were collected. As observed, the SERS intensity plots at respective peaks of 832 and 1109 cm^{-1} exhibit minimal fluctuations, with RSD values of 2.7% and 1.9%, respectively (Figure 6c). Under conditions of uniform molecular distribution, even weakly adsorbed molecules demonstrate high reproducibility and reliability. Due to the uniform distribution of molecules, the probability of detecting signals on SHB/SHL modified substrates remains around 20% even at a concentration of 10^{-9} M (Figure 6d). In contrast, on the HANM structure, the few molecules in low-concentration solutions predominantly gather in the coffee ring area, with most of the central region having fewer molecules. This results in only a 50% detection probability at 10^{-7} M, which sharply decreases as the concentration decreases, significantly hindering rapid and accurate detection. On the other hand, consistent with previously obtained results, the outstanding homogeneity of the HANM-SHB/SHL structure leads to an excellent linear relationship between molecular concentration and SERS intensity. The BPA SERS spectra from 10^{-5} to 10^{-9} M are shown in Figure S11b, where R^2 for the peak intensities at 832 and 1109 cm^{-1} reach 0.996 and 0.988 (Figure 6e), respectively. These results indicate that the

https://doi.org/10.1021/acs.analchem.4c05301
Anal. Chem. 2024, 96, 20612−20621

HANM-SHB/SHL structure can provide consistent and reliable quantitative analysis over a broad concentration range, further demonstrating their superior performance in practical applications.

To further evaluate the practical application potential of the HANM-SHB/SHL structure, BPA detection was conducted on water samples collected from five different locations (Figure 6f). The sampling points included Qingdao' adjacent Huanghai Sea, Weihai' adjacent Huanghai Sea, Dongying' adjacent Bohai Sea, Dongping Lake, and Weishan Lake. These locations varied in geographical position and water quality, representing different environmental backgrounds, which helped to comprehensively assess the practical performance of the modified substrates. Equal concentrations of BPA were spiked into the water samples at each sampling point and tested for SERS using the HANM and HANM-SHB/SHL structures, respectively. Figure 6f illustrates the boxplot distribution of the SERS intensities at 832 cm^{-1} for 10 spectra taken randomly from each of the five sampling points on the HANM-SHB/SHL structure. The corresponding SERS spectra can be seen in Figure S11c. The RSDs for five sampling points are 2.9%, 5.6%, 3.5%, 1.6%, and 2.6%, respectively. Despite differences in water quality at the sampling points, the HANM-SHB/SHL structure consistently detected BPA in all water samples with a good signal intensity uniformity. This indicates that SHB/SHL modified substrates possess excellent environmental adaptability and detection sensitivity. Specifically, in water samples from Dongping Lake and Weishan Lake, the SERS intensity distribution was relatively concentrated, indicating a stable and reproducible detection performance in these freshwater lakes. In the Bohai and Huanghai Sea sampling points, the presence of higher salinity and complex matrices in seawater caused slight fluctuations in the detection signal distribution, but the HANM-SHB/SHL structure was still effective in detecting BPA.

In addition, the SERS spectra of BPA detection using the HANM structure on water samples from five different locations are shown in Figure S12a. For the five samples with different water qualities, the relative standard deviations (RSDs) of the intensities of 10 randomly collected spectra at 832 cm^{-1} were 9.2%, 11.5%, 15.1%, 7.6%, and 7.1%, respectively (Figure S12b). The results indicate that, whether in high-salinity, complex seawater samples, or relatively clean freshwater samples, the signal intensity fluctuations at BPA dry spots were significantly larger compared to those obtained with the HANM-SHB/SHL structure. These data demonstrate that SHB/SHL modification provides a notable advantage over the use of HANM alone in practical detection.

Overall, the HANM-SHB/SHL structure offers a promising solution for enhancing SERS detection of weakly adsorbed molecules such as BPA. They are capable of producing uniform molecular distributions, providing high-intensity signals, and delivering reliable quantitative data, making them valuable tools for environmental monitoring and other applications requiring high sensitivity and precise molecular detection. With further optimization and large-scale application, SHB/SHL modified substrates are expected to play a crucial role in real-world pollutant monitoring, providing effective technical support for environmental protection and pollution control.

CONCLUSION

In summary, we propose an innovative sensing strategy that leverages HANM and SHB/SHL surface treatments, addressing both structural and molecular deposition aspects for achieving uniformity and quantitative analysis in SERS detection. The combined HANM structure not only enhances the interaction between light and molecules but also expands the generation area of the hottest spots, significantly boosting the intensity and quantitative detection capability of the SERS signals. The treatment of SHB/SHL interactive surfaces not only efficiently enriches the target elements in the sample solution but also arranges the analytes in an array format, meeting the demands of high-throughput detection. Most crucially, the successful avoidance of the coffee ring effect by the SHB/SHL interactive surface ensures an even distribution of molecules at the target sites. Even at low concentrations (e.g., R6G at 10^{-12} M), a high level of uniformity is maintained, providing favorable conditions for quantitative detection. The performance of this strategy inspires our continuous pursuit of high-performance analytical tools. We believe that this diversified and comprehensive sensing strategy will exhibit extensive application prospects in biomedical research, environmental monitoring, and other fields, offering more precise and reliable analytical means for biosensing studies and practical applications.

ASSOCIATED CONTENT

Supporting Information

The Supporting Information is available free of charge at https://pubs.acs.org/doi/10.1021/acs.analchem.4c05301.

Schematic diagram of PS microsphere array preparation; optical image of HANM structure; contact angle images of HANM structure under various modification conditions; appearance and related characteristics of AM structures at different growth times; appearance of AM structures at different growth temperatures; size distributions of nanosheet and nanoholes respectively; top view of an optical image of droplet evaporation under various modification conditions; 200 SERS spectra collected on the HANM-SHB/SHL and HANM structure; SERS spectra of CV molecular-related properties collected on the HANM-SHB/SHL structure; SERS spectra of BPA molecular-related properties collected on the HANM-SHB/SHL structure (PDF)

Movie 1: The analytical solution could be stably confined to the SERS detection site and would not shift even if inverted (MP4)

Movie 2: The proposed SERS platform with HANM-SHB/SHL structure can achieve automatic sampling and high throughput detection (MP4)

AUTHOR INFORMATION

Corresponding Authors

Zhen Li − *School of Physics and Electronics, Shandong Normal University, Jinan 250014, China;* orcid.org/0000-0002-6820-4187; Email: sdnuzhenli@126.com

Chao Zhang − *School of Physics and Electronics, Shandong Normal University, Jinan 250014, China;* orcid.org/0000-0002-3295-8980; Email: czsdnu@126.com

Authors

Tiying Zhu − *School of Physics and Optoelectronic Engineering, Beijing University of Technology, Beijing 100124, China; School of Physics and Electronics, Shandong Normal University, Jinan 250014, China*

https://doi.org/10.1021/acs.analchem.4c05301
Anal. Chem. 2024, 96, 20612−20621

Zhiyang Pei − *School of Physics and Electronics, Shandong Normal University, Jinan 250014, China*
Xiaofei Zhao − *School of Physics and Electronics, Shandong Normal University, Jinan 250014, China;* orcid.org/0000-0002-3714-9621
Jing Yu − *School of Physics and Electronics, Shandong Normal University, Jinan 250014, China*
Baoyuan Man − *School of Physics and Electronics, Shandong Normal University, Jinan 250014, China*
Pingheng Tan − *State Key Laboratory of Superlattices and Microstructures, Institute of Semiconductors, Chinese Academy of Sciences, Beijing 100083, China;* orcid.org/0000-0001-6575-1516

Complete contact information is available at: https://pubs.acs.org/10.1021/acs.analchem.4c05301

Notes

The authors declare no competing financial interest.

■ ACKNOWLEDGMENTS

The authors are grateful for financial support from the National Natural Science Foundation of China (Grants 12174229 and 12004226), Taishan Scholars Program of Shandong Province (Grant tsqn202306152), Qingchuang Science and Technology Plan of Shandong Province (Grant 2021KJ006), and Shandong Provincial Natural Science Foundation (Grant ZR2022YQ02).

■ REFERENCES

(1) Langer, J.; Jimenez De Aberasturi, D.; Aizpurua, J.; Alvarez-Puebla, R. A.; Auguié, B.; Baumberg, J. J.; Bazan, G. C.; Bell, S. E.; Boisen, A.; Brolo, A. G.; et al. *ACS Nano* **2020**, *14*, 28−117.
(2) Hang, Y.; Boryczka, J.; Wu, N. *Chem. Soc. Rev.* **2022**, *51*, 329−375.
(3) Xu, Y.; Zhang, Y.; Li, C.; Ye, Z.; Bell, S. E. *Acc. Chem. Res.* **2023**, *56*, 2072−2083.
(4) Shao, M.; Ji, C.; Tan, J.; Du, B.; Zhao, X.; Yu, J.; Man, B.; Xu, K.; Zhang, C.; Li, Z. *Opto-Electron. Adv.* **2023**, *6*, 230094.
(5) Tan, J.; Du, B.; Ji, C.; Shao, M.; Zhao, X.; Yu, J.; Xu, S.; Man, B.; Zhang, C.; Li, Z. *Acs Photonics* **2023**, *10* (7), 2216−2225.
(6) Pei, Z.; Li, J.; Ji, C.; Tan, J.; Shao, Z.; Zhao, X.; Li, Z.; Man, B.; Yu, J.; Zhang, C. *J. Phys. Chem. Lett.* **2023**, *14* (25), 5932−5939.
(7) Altug, H.; Oh, S.; Maier, S. A.; Homola, J. *Nat. Nanotechnol.* **2022**, *17*, 5−16.
(8) Guo, J.; Zeng, F.; Guo, J.; Ma, X. *J. Mater. Sci. Technol.* **2020**, *37*, 96−103.
(9) Hajikhani, M.; Zhang, Y.; Gao, X.; Lin, M. *Trends Food Sci. Technol.* **2023**, *138*, 615.
(10) Ko, H.; Singamaneni, S.; Tsukruk, V. V. *Small* **2008**, *4*, 1576−1599.
(11) Li, C.; Zhang, Y.; Ye, Z.; Bell, S. E.; Xu, Y. *Nat. Protoc.* **2023**, *18*, 2717−2744.
(12) Ding, Q.; Wang, J.; Chen, X.; Liu, H.; Li, Q.; Wang, Y.; Yang, S. *Nano Lett.* **2020**, *20*, 7304−7312.
(13) Chen, X.; Huang, Q.; Ruan, S.; Luo, F.; You, R.; Feng, S.; Zhu, L.; Wu, Y.; Lu, Y. *Anal. Chim. Acta* **2022**, *1227*, No. 340302.
(14) Niemeyer, C. M. *Angew. Chem., Int. Ed.* **2001**, *40*, 4128−4158.
(15) Yunker, P. J.; Still, T.; Lohr, M. A.; Yodh, A. G. *Nature* **2011**, *476*, 308−311.
(16) Zhang, D.; Peng, L.; Shang, X.; Zheng, W.; You, H.; Xu, T.; Ma, B.; Ren, B.; Fang, J. *Nat. Commun.* **2020**, *11*, 2603.
(17) Neto, M. D.; Stoppa, A.; Neto, M. A.; Oliveira, F. J.; Gomes, M. C.; Boccaccini, A. R.; Levkin, P. A.; Oliveira, M. B.; Mano, J. F. *Adv. Mater.* **2021**, *33*, No. 2007695.
(18) Feng, J.; Qiu, Y.; Jiang, L.; Wu, Y. *Adv. Mater.* **2022**, *34*, No. 2106857.
(19) Pal, A.; Gope, A.; Sengupta, A. *Adv. Colloid Interface Sci.* **2023**, *314*, No. 102870.
(20) Liang, S.-J.; Mao, J.-K.; Gong, C.; Yu, D.-D.; Zhou, J.-G. *Chin. J. Anal. Chem.* **2019**, *47*, 1878−1886.
(21) Gao, Y.; Zhu, H.; Wang, X.; Shen, R.; Zhou, X.; Zhao, X.; Li, Z.; Zhang, C.; Lei, F.; Yu, J. *Small* **2023**, *19*, No. 2207324.
(22) Huang, F. M.; Wilding, D.; Speed, J. D.; Russell, A. E.; Bartlett, P. N.; Baumberg, J. J. *Nano Lett.* **2011**, *11*, 1221−1226.
(23) Liu, M.; Feng, L.; Zhang, X.; Hua, Y.; Wan, Y.; Fan, C.; Lv, X.; Wang, H. *ACS Appl. Mater. Interfaces* **2018**, *10* (38), 32038−32046.
(24) Sau, T. K.; Rogach, A. L. *Adv. Mater.* **2010**, *22*, 1781−1804.
(25) Kumar, S.; Pande, S.; Verma, P. *Int. J. Curr. Eng. Technol.* **2015**, *5*, 700−703.
(26) Park, S. K.; Kim, Y.; Han, J. *Org. Electron.* **2009**, *10*, 1102−1108.
(27) Xue, C.; Yang, K. *J. Colloid Interface Sci.* **2010**, *344*, 48−53.
(28) Asano, H.; Shiraishi, Y. *Anal. Chim. Acta* **2015**, *883*, 55−60.
(29) Bera, L. K.; Soo, O. K.; Zheng, W. Z. *Rsc Adv.* **2014**, *4*, 38384−38388.
(30) Van Gaalen, R. T.; Diddens, C.; Wijshoff, H.; Kuerten, J. *J. Colloid Interface Sci.* **2021**, *584*, 622−633.
(31) Wang, Z.; Orejon, D.; Takata, Y.; Sefiane, K. *Phys. Rep.* **2022**, *960*, 1−37.
(32) Natan, M. J. *Faraday Discuss.* **2006**, *132*, 321−328.
(33) Aung, M. T.; Shimabuku, K. K.; Soares-Quinete, N.; Kearns, J. P. *Water Res.* **2022**, *213*, No. 118146.
(34) Pignatello, J. J.; Mitch, W. A.; Xu, W. *Environ. Sci. Technol.* **2017**, *51*, 8893−8908.

Supporting Information

Advanced SERS Platform for Uniform and Reliable Molecular Detection

Tiying Zhu[a,b], Zhiyang Pei[b], Xiaofei Zhao[b], Jing Yu[b], Baoyuan Man[b], Pingheng Tan[c], Zhen Li[b] and Chao Zhang[b*]*

[a] *School of Physics and Optoelectronic Engineering, Beijing University of Technology, Beijing, 100124, China*

[b] *School of Physics and Electronics, Shandong Normal University, Jinan 250014, China*

[c] *State Key Laboratory of Superlattices and Microstructures, Institute of Semiconductors, Chinese Academy of Sciences, Beijing 100083, China*

[*]E-mail: czsdnu@126.com, Chao Zhang
sdnuzhenli@126.com, Zhen Li

Contents

Fig. S1. Schematic diagram of PS microsphere array preparation

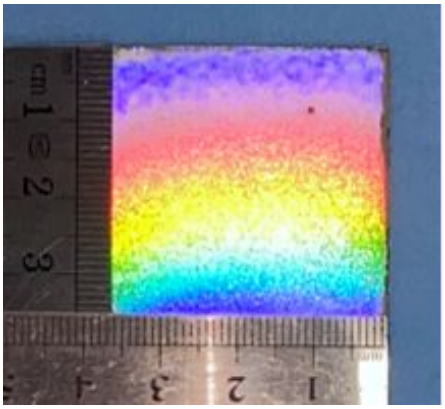

Fig. S2. Optical image of 3.5cm^2 Ag nanopores-microbowls substrate

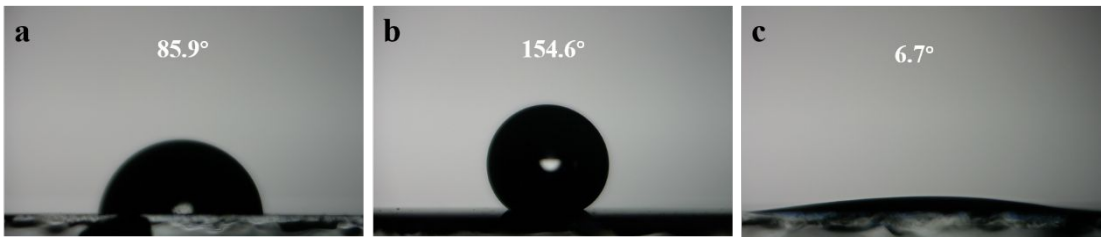

Fig. S3. Contact angle image of (a) the HANM structure, (b) the HANM-SHL structure and (c) the HANM-SHB structure.

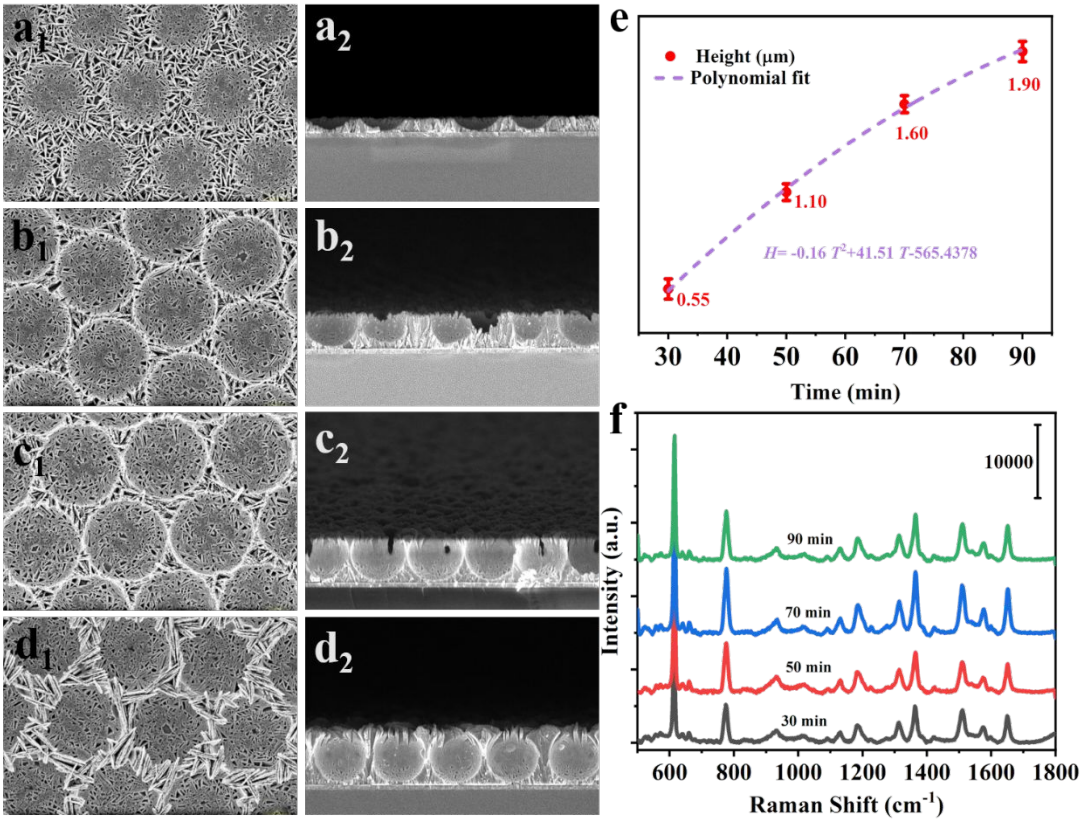

Fig. S4. SEM images of AM structure prepared when the growth times were (a_1 and a_2) 30 min, (b_1 and b_2) 50 min, (c_1 and c_2) 70 min and (d_1 and d_2) 90min. (e) The growth height versus time of the AM structure. (f) SERS spectra collected from AM structure prepared under different growth times.

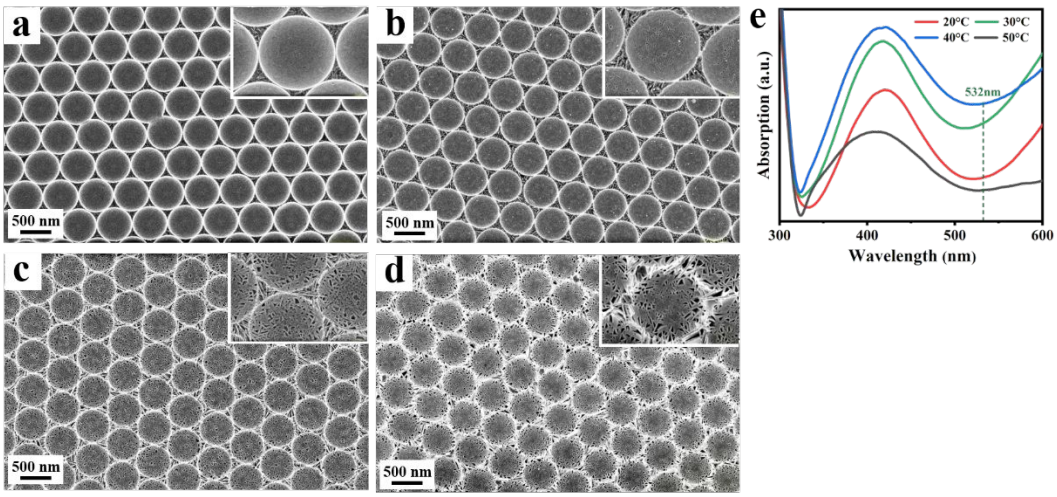

Fig. S5. SEM images of AM structure prepared when the electrolyte t emperatures were (a) 20°C, (b) 30°C, (c) 40°C and (d) 50°C. (e) Absorption spectra of AM structures prepared at different growth temperatures

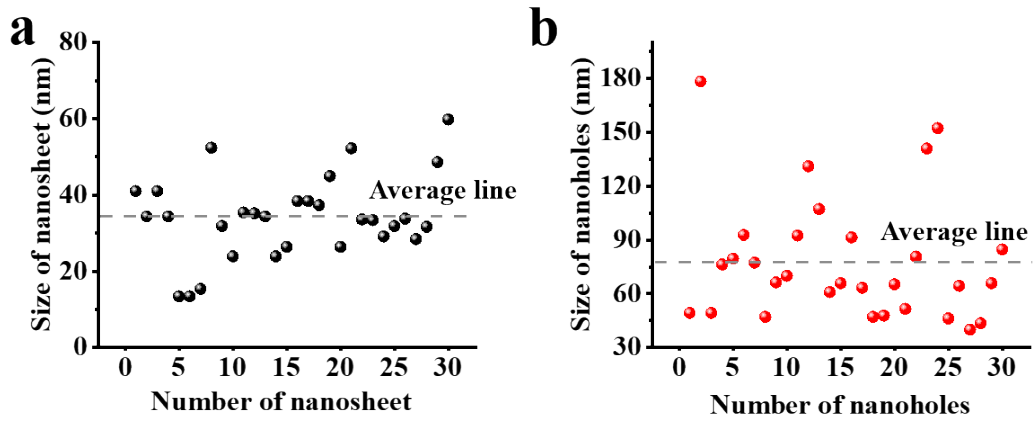

Fig. S6. (a)and (b) are Size distributions of nanosheet and nanoholes respectively

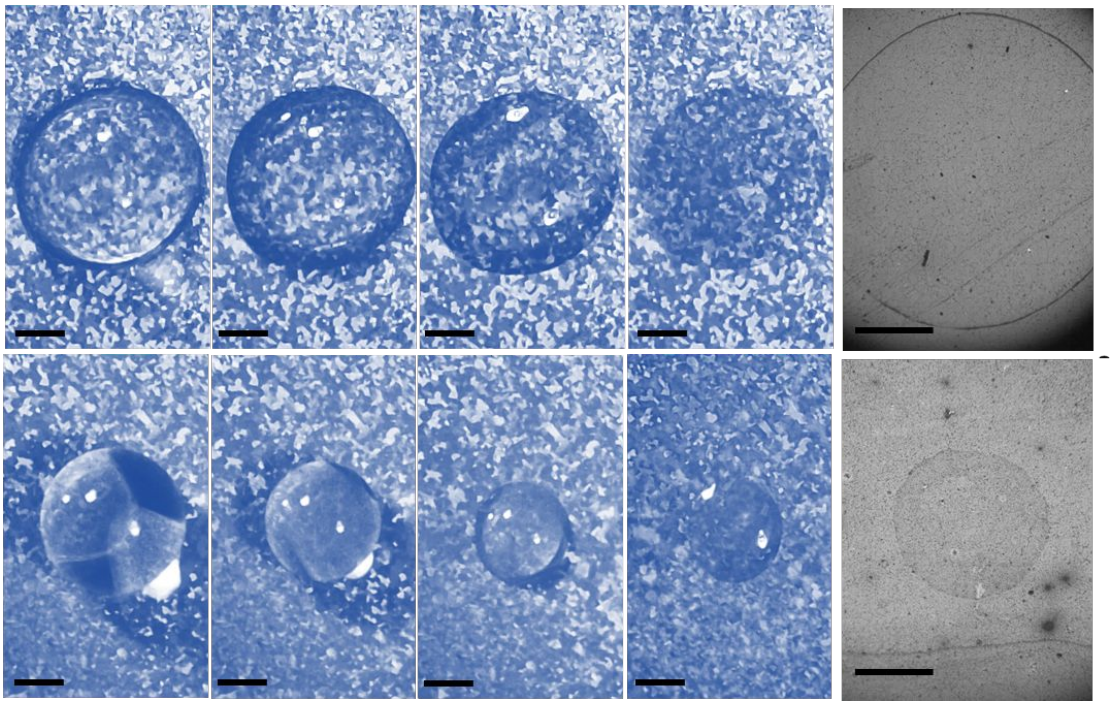

Fig. S7. Top view of an optical image of droplet evaporation on the HANM structure and HANM-SHB/SHL structure (The scale is 500 μm).

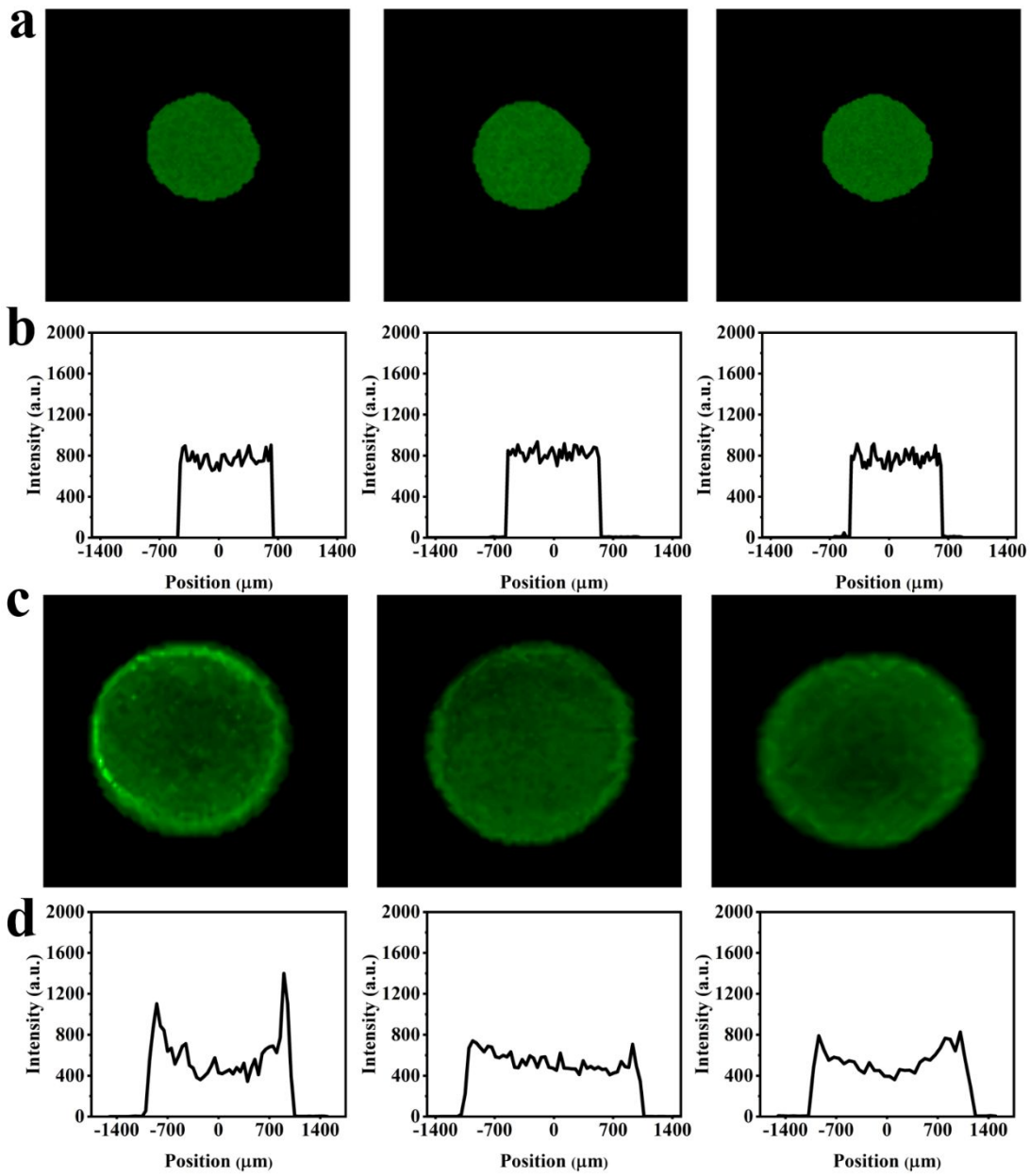

Fig.S8. SERS mapping of 4 μL R6G droplets at a concentration of 10^{-10} M at 613 cm^{-1} obtained from three different batches of (a)the HANM-SHB/SHL structure, (c) the HANM structure. (b) and (d) are the SERS intensities of the corresponding (a) and (c).

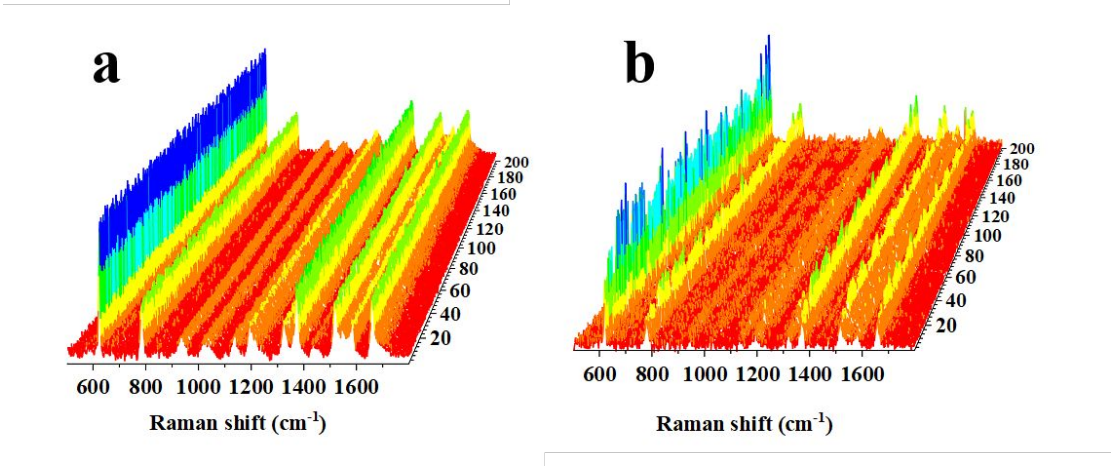

Fig. S9. 200 SERS spectra for R6G molecules at concentrations of 10^{-10} M on the HANM-SHB/SHL structure and the HANM structure.

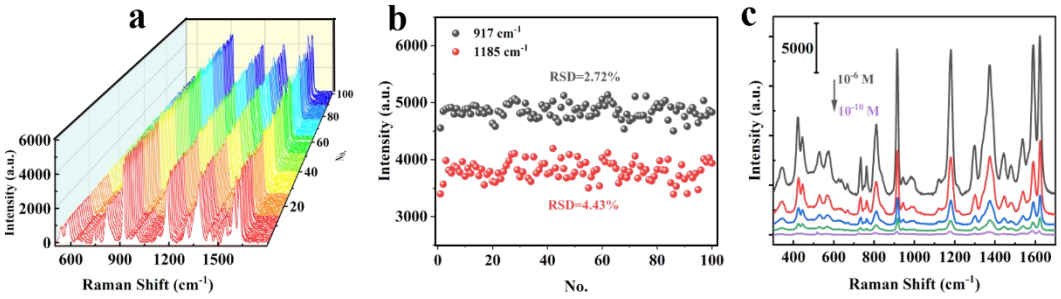

Fig. S10. (a) 100 SERS spectra for CV molecules at concentrations of 10^{-6} M on the HANM-SHB/SHL structure. (b) 100 intensity scatter plots at 917 cm^{-1} and 1185 cm^{-1}. (c) SERS spectra of CV at concentrations of 10^{-6} M-10^{-10} M.

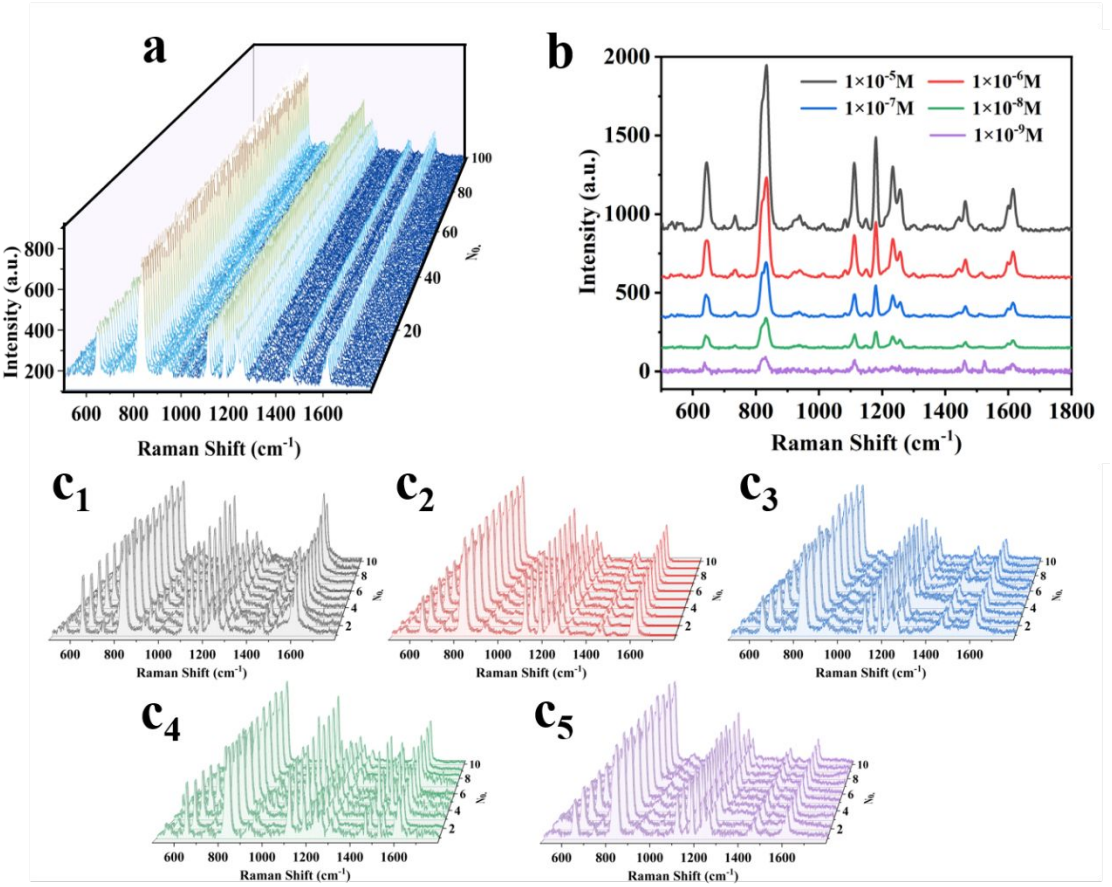

Fig.S11. (a) 100 SERS spectra for BPA molecules at concentrations of 10^{-6} M on the HANM-SHB/SHL structure. (b) SERS spectra of BPA at concentrations of 10^{-5} M-10^{-9} M. SERS spectra of BPA in water samples from five different locations using the HANM-SHB/SHL structure: (c_1) Qingdao' adjacent Huanghai Sea, (c_2) Weihai' adjacent Huanghai Sea, (c_3) Dongying' adjacent Bohai Sea, (c_4) Dongping Lake, (c_5) Weishan Lake.

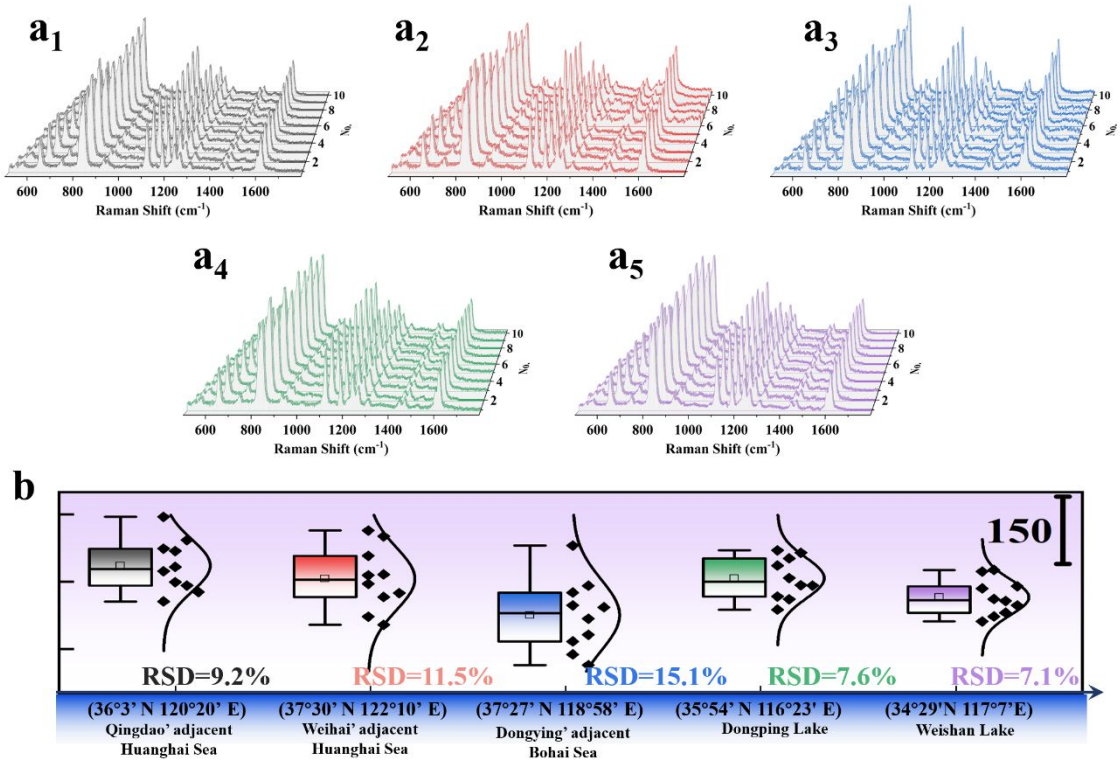

Fig.S12. SERS spectra of BPA in water samples from five different locations using the HANM-SHB/SHL structure: (a_1) Qingdao' adjacent Huanghai Sea, (a_2) Weihai' adjacent Huanghai Sea, (a_3) Dongying' adjacent Bohai Sea, (a_4) Dongping Lake, (a_5) Weishan Lake. (b) Corresponding SERS intensity distribution at 832 cm^{-1} for the spectra in (a_1-a_5).